Materials Today Chemistry 40 (2024) 102194

Contents lists available at ScienceDirect

Materials Today Chemistry

journal homepage: www.journals.elsevier.com/materials-today-chemistry/

High-capacitance $BiPO_4$ material with monoclinic/hexagonal crystalline phase heterostructure for aqueous asymmetric supercapacitors

Min Li [a,b], Mingshu Zhao [a,**], Bing Wu [b], Shuangying Wei [b], Stefanos Mourdikoudis [b], Vlastimil Mazánek [b], Lukas Dekanovsky [b], Filipa M. Oliveira [b], Jalal Azadmanjiri [b], Zdeněk Sofer [b,*]

[a] School of Physics, Key Laboratory of Shaanxi for Advanced Functional Materials and Mesoscopic Physics, MOE Key Laboratory for Nonequilibrium Synthesis and Modulation of Condensed Matter, Xi'an Jiaotong University, Xi'an, 710049, Shaanxi, China
[b] Department of Inorganic Chemistry, University of Chemistry and Technology Prague, Technická 5, 16628, Prague, Czech Republic

ARTICLE INFO

Keywords:
Bismuth phosphate
Heterostructure
Cobalt-nickel phosphate
Aqueous asymmetric supercapacitor

ABSTRACT

Aqueous asymmetric supercapacitor devices generally have a fairly high power density, but their practical application is still limited by low energy density due to lack of high-capacity electrode materials, particularly anode materials. Herein, a novel anode material, $BiPO_4$ material with monoclinic/hexagonal crystalline phase heterostructure was synthesized by a simple solvothermal approach. This unique heterostructure, composed of hexagonal and monoclinic nanoparticles, exhibits a large specific surface area, numerous active sites and high ion diffusion rate, all of which contribute to an enhanced specific capacitance in the energy storage process. Besides, the heterogeneous interface formed between two different crystalline phase nanoparticles is regarded as an excellent ion channel, accelerating diffusion and reaction of electrolyte ions. The acquired $BiPO_4$ material serves as anode for aqueous supercapacitors, displaying a superior specific capacitance of 954 F g^{-1} (265 mAh g^{-1}) at 1 A g^{-1} current density, maintaining up to 600 F g^{-1} (166.7 mAh g^{-1}) at 10 A g^{-1}. In order to match the $BiPO_4$ anode, high-capacity (3662 F g^{-1} (508.61 mAh g^{-1}) at 1 A g^{-1}) cobalt-nickel phosphate micron-sheets ($NiCo_2(PO_4)_2$) synthesized *via* hydrothermal method followed by calcination under argon were selected as cathode material. The assembled aqueous asymmetric supercapacitor employing $NiCo_2(PO_4)_2$ as cathode and $BiPO_4$ as anode yields a high energy density of 98.17 Wh kg^{-1} at a power density of 846.49 W kg^{-1}.

1. Introduction :

The depletion of energy resources and the resulting environmental pollution have become major concerns worldwide, as modern societies rely heavily on non-renewable energy sources like oil and natural gas. To address these issues, rechargeable batteries and supercapacitors, comprising recyclable green energy storage systems, are becoming increasingly popular as energy storage solutions in daily life [1–3]. Lithium-ion batteries (LIBs) are well-known for their excellent performance characteristics, including high voltage, high capacity and high energy density. Still, the relative scarcity of lithium element and safety issues related to the organic electrolyte are puzzling drawbacks. As a result, research on aqueous energy storage devices with aqueous electrolyte, such as supercapacitors with higher power density and rechargeable lithium/sodium/zinc ion batteries, has increased due to their higher safety, environmentally benign nature and lower cost of aqueous electrolyte [4–6]. In fact, electrical double-layer capacitors (EDLCs) possess high power density and long cycle life, but their lower discharge specific capacitance and energy density limit their market competitiveness. The use of asymmetric supercapacitors (ASCs) can tackle this issue usually by combining battery-type materials with faradaic reaction as cathode and capacitive materials as anode, which widens the voltage window and increases the energy density of the ASCs [7,8].

The ASCs are usually constructed by cathode materials such as transition-metal oxides ($NiO/MnO_2/Fe_2O_3/NiCo_2O_4$) [9–12], hydroxides ($Co(OH)_2/Ni(OH)_2$) [13,14], sulfides ($NiS_2/Ni_3S_2/Co_9S_8/MoS_2$) [15–18], phosphides (CoP/Ni_2P/FeP) [19–21] as well as phosphate

* Corresponding author.
** Corresponding author.
E-mail addresses: zhaomshu@xjtu.edu.cn (M. Zhao), zdenek.sofer@vscht.cz (Z. Sofer).

https://doi.org/10.1016/j.mtchem.2024.102194
Received 29 March 2024; Received in revised form 6 July 2024; Accepted 10 July 2024
Available online 24 July 2024

composites ($Mn_3(PO_4)_2{\cdot}3H_2O/Co_3(PO_4)_2{\cdot}8H_2O/Ni_3(PO_4)_2{\cdot}8H_2O$) [22–24], and anode materials (see Fig. S1) including carbon-based materials (activated carbon (AC), carbon nanotubes (CNTs) and graphene oxide (GO), among others) [25,26] as well as metal-based materials. Based on previous literatures, a diverse range of high-capacity cathode materials have been applied in asymmetric supercapacitor devices, while the research of their anode counterparts mainly focuses on carbon-based materials. Although carbon-based materials as anode electrode materials can improve the cycle stability of supercapacitors, the enhancement of energy density for devices is largely restricted due to its inherently low theoretical capacity. Surprisingly, there have been plenty of promising anode electrode materials for ASCs in recent years, and their historical development timeline is presented in Fig. S2. Among them, the emerging bismuth phosphate material has inherent redox-active ions, high theoretical capacity, and a quite low potential, thus appearing as a competitive candidate in the field of anode materials for aqueous ASCs [27,28]. However, despite its potential, bismuth phosphate is also a typical semiconductor material with a wide band gap, which results in poor electronic conductivity. This limits the oxidation and reduction reaction rate and negatively impacts its electrochemical performance. To tackle this issue, S. Vadivel et al. utilized a solvothermal approach to synthesize $BiPO_4$/MWCNT, incorporating multi-walled carbon nanotubes (MWCNT) as a carbon source [29]. The resulting $BiPO_4$/MWCNT composite showed a specific capacitance of 504 F g^{-1} at 5 mV s^{-1}, due to the improvement of electrical conductivity. $BiPO_4$ produced by V.D. Nithya et al. exhibits a significantly improved specific capacitance (202 F g^{-1} at 5 mA cm^{-2}) under hexamethylenetetramine (HMT) assistance, attributed to the smaller particle size caused by adding different concentration of HMT [30]. Prakash Chand et al. fabricated a nanostructured $BiPO_4$ material employing a fast microwave irradiation method [31]: their results demonstrated that nanostructured $BiPO_4$ possesses excellent electrochemical properties (610 C g^{-1} at 2 A g^{-1}). In addition, other improved approaches, including the adjustment of the pH value of the solution, using different synthesis methods, and generating diverse morphologies, have been attempted to boost the electrochemical performance of bismuth phosphate materials [32–34]. Even though the electrochemical properties of $BiPO_4$ have been significantly enhanced as a result of various ameliorated synthetic routes, they have not yet reached an adequate level which would enable their real-world practical use. Therefore, the development of bismuth phosphate materials with higher performance is of paramount significance.

In accordance with what has been learned from earlier studies [35], we have rationally designed and synthesized bismuth phosphate materials with hexagonal and monoclinic heterostructures, inspired by its inherent characteristics with various crystalline phases. The capacitance of the bismuth phosphate material is significantly improved, as this heterostructure effectively increases the diffusion rate of OH^- inside the electrode material. The diffusion coefficient of OH^- ($\sim 10^{-4}$ cm^2 s^{-1}) within BP150 is larger compared to that of the single crystalline phase phosphate materials ($\sim 10^{-9}$ and $\sim 10^{-8}$) [36,37]. To the best of our knowledge, there have been few reports about the preparation of hexagonal/monoclinic phase $BiPO_4$ for aqueous supercapacitors. In addition, we have thoroughly characterized and analyzed the internal relationship between the temperature and solvent changes of bismuth phosphate material and the crystal phase transition during the synthesis of bismuth phosphate material, aas well as their effect on the electrochemical performance.

The high-capacitance cobalt-nickel phosphate ($NiCo_2(PO_4)_2$) produced through a hydrothermal route followed by annealing under argon (Ar) atmosphere was employed as a cathode paired with $BiPO_4$ anode. The assembled $NiCo_2(PO_4)_2$//$BiPO_4$-150 asymmetric supercapacitor (ASC) displayed a high energy density of 98.17 Wh kg^{-1} at a power density of 846.49 W kg^{-1}, while even at a high power density of 6735.43 W kg^{-1}, the energy density was still at 39.29 Wh kg^{-1}. Compared to other materials reported so far in the literature, the energy density of the present material is particularly competitive and promising for a wide range of further studies and exploitation.

2. Experimental

2.1. Materials and chemicals

Bismuth(III) nitrate pentahydrate ($Bi(NO_3)_3{\cdot}5H_2O$, Fluka); disodium hydrogen phosphate dehydrate ($Na_2HPO_4{\cdot}2H_2O$, Lachner); cobalt(II) nitrate hexahydrate ($Co(NO_3)_2{\cdot}6H_2O$, Lachema); nickel(II) nitrate hexahydrate ($Ni(NO_3)_2{\cdot}6H_2O$, Penta); poly-(vinylidene fluoride) (PVDF, Alfa Aesar); N-methylpyrrolidone (NMP, 99.7 %, Sigma-Aldrich); ethanol (C_2H_5OH, 99.8 %, Penta). The nickel foam substrate (99.9 %, 350 ± 20 g/m^2) was bought from TMAX company. All reagents used are of analytical grade and without further purification.

2.2. Synthesis of $BiPO_4$ heterostructure

2 mmol $Bi(NO_3)_3{\cdot}5H_2O$ was added to a mixed solution of 20 mL ethylene glycol and 10 mL ethanol under magnetic stirring to obtain transparent solution A. Simultaneously, 2 mmol $Na_2HPO_4{\cdot}2H_2O$ was dissolved in 10 mL of deionized water with magnetic stirring for 10 min to obtain a clear solution, named as solution B. Solution B was then slowly dropped to solution A with continuous stirring for 1 h, leading to the formation of a white emulsion. The resulting mixture was then transferred to a 100 mL sealed Teflon-lined autoclave and kept at 150 °C for 12 h in an electric oven. The obtained precipitates were rinsed alternately with deionized water and ethanol for three times, and dried for 6 h at 60 °C in a vacuum oven. The final product was named as $BiPO_4$-150 °C (BP150). For comparison, the same solvothermal reaction process was performed with different reaction temperatures (80, 120, 165 and 180 °C), and the acquired $BiPO_4$ was listed as BP80, BP120, BP165 and BP180, respectively. Furthermore, the samples BP80 and BP180 were physically mixed at a mass ratio of 1:1 and named as Mixed.

2.3. Synthesis of cobalt-nickel phosphate on nickel foam

The high-capacitance cobalt-nickel phosphate binary metal material grown directly on nickel foam (NF) was synthesized by hydrothermal method combined with calcination under argon atmosphere. The synthesized cobalt nickel phosphate materials were named $NiCo_2(PO_4)_2$-300 (NCP-300), $NiCo_2(PO_4)_2$-350 (NCP-350), $NiCo_2(PO_4)_2$-400 (NCP-400), respectively, according to their distinct calcination temperature.

2.4. Fabrication of the aqueous asymmetric supercapacitor

The asymmetric supercapacitors were assembled by using cobalt-nickel phosphate material (NCP-350) as cathode electrode, bismuth phosphate (BP150) as anode electrode, and 3 M KOH aqueous solution as electrolyte.

2.5. Materials characterizations

X-ray powder diffraction (XRD) measurements (Bruker D8 Discoverer powder diffractometer, Cu Kα radiation (U = 40 kV, I = 40 mA)) were recorded at a range of 2θ from 10° to 70°. The morphology of samples was characterized using a scanning electron microscope (SEM) (SEM, Tescan Lyra 3, Czech Republic) equipped with an energy-dispersive X-ray spectroscopy (EDX) (Oxford instruments 80). The SEM and EDX measurements were carried out using 5 and 10 kV accelerating voltages, respectively. The microstructure of the samples was studied by transmission electron microscopy (TEM) using an EFTEM JEOL 2200 FS microscope at an accelerating voltage of 200 keV (JEOL, Japan). The specific surface areas of the samples were calculated *via* the Brunauer–Emmett–Teller (BET) method, and the Barrett–Joyner–Halenda (BJH) algorithm was employed to determine pore

size distributions from isotherms. The functional groups and vibration modes of materials were analyzed by Fourier Transform Infrared (FTIR) spectroscopy (FTIR-ATR, NICOLET iS50R, Czech Republic).

2.6. Electrochemical measurement

Electrochemical characterization was carried out using a three-electrode system in a 3 M KOH electrolyte. The active material, Pt foil and Hg/HgO electrode served as working electrode (WE), counter electrode and reference electrodes, respectively. The WE was prepared by coating a nickel foam (1 × 1 cm^2) with a ratio of 80 wt% active material, 10 wt% acetylene black and 10 wt% poly(vinylidene fluoride) (PVDF) in N-methyl pyrrolidone (NMP) solvent, and dried in a vacuum at 100 °C for 12 h. The mass loading of the WE was approximately 2.4–3 mg cm^{-2}. Galvanostatic charging-discharging (GCD), cyclic voltammetry (CV) tests, and electrochemical impedance spectroscopy (EIS) measurements were performed on Autolab PGSTAT 204 (Metrohm, Switzerland) at room temperature. The cycle performance test was recorded by a Neware battery test system (BTX 7.6, Shenzhen, China). GCD and CV tests of active material were performed in the voltage window from −1 to 0 V *vs.* Hg/HgO. The following formula was employed to determine the specific capacitance:

$$C\ (F\ g^{-1}) = I\ \Delta t\ /\ m\ \Delta V \tag{1}$$

$$C\ (mAh\ g^{-1}) = I\ \Delta t\ /\ 3.6\ m \tag{2}$$

where I, Δt, m and ΔV represent discharge current (A), discharge time (s), mass loading (mg) and voltage (V), respectively.

The ASC was assembled by using $NiCo_2(PO_4)_2$ (NCP-350) as the cathode, BP150 as the anode, and 3 M KOH as the electrolyte in the voltage range of 0~1.6 V, while the optimal operating temperature range for the NCP-350//BP150 ASC device is between 20 °C and 45 °C. According to the charge balance principle ($q^+ = q^-$), the mass loading of the cathode and anode was confirmed by the formula:

$$m^+ / m^- = C^- V^- / C^+ V^+ \tag{3}$$

Based on the following formula, the energy density (E) and power density (P) of the ASC can be acquired:

$$E\ (Wh\ kg^{-1}) = I \int v dt \Big/ 3.6m \tag{4}$$

$$P\ (W\ kg^{-1}) = E / \Delta t \tag{5}$$

where *I*, *t* and *v* stand for current density (A g^{-1}), discharge time (s) and working voltage (V) of the ASC device.

3. Results and discussion

The flowchart for the preparation of BP150 is shown in Fig. 1a, demonstrating that BP150 nanomaterial synthesized at a temperature of 150 °C exhibited well-dispersed and uniform nanostructures with a regular anisotropic growth pattern. Notably, it is of importance to select the optimal reaction temperature, solvent and time for $BiPO_4$ materials, as this can affect the formation of different crystal phases, the overall morphology and internal microstructure of the produced material.

The crystal structure and phase of the synthesized samples were investigated by XRD measurements, as displayed in Fig. 1b, indicating that all samples exhibit sharp diffraction peaks and no impurities are present. Typically, bismuth phosphate materials have three distinct crystalline forms, involving hexagonal, low-temperature monoclinic and high-temperature monoclinic phases [38]. The diffraction peak of BP80 matches well with that of hexagonal phase (JCPDS Card NO. 15–0766), and the formation of the hydrated hexagonal phase is ascribed to the low reaction temperature employed during synthesis. Interestingly, the diffractograms of BP120 , BP150 and BP165 imply the presence of both hexagonal and low-temperature monoclinic phases (JCPDS Card No. 15–0766 and 16–4363). The reasoning behind such observation is probably associated with the increased reaction temperature; this would have led to partial dehydration of hexagonal phase and its conversion into monoclinic crystal structure in those samples. The hexagonal phase of bismuth phosphate is composed of PO_4 tetrahedra units and BiO_8 polyhedra units, and the edges of BiO_8 polyhedra units are shared with hexagonal channels occupied by water. As the synthesis temperature increases, PO_4 tetrahedra in the crystal structure of bismuth phosphate is

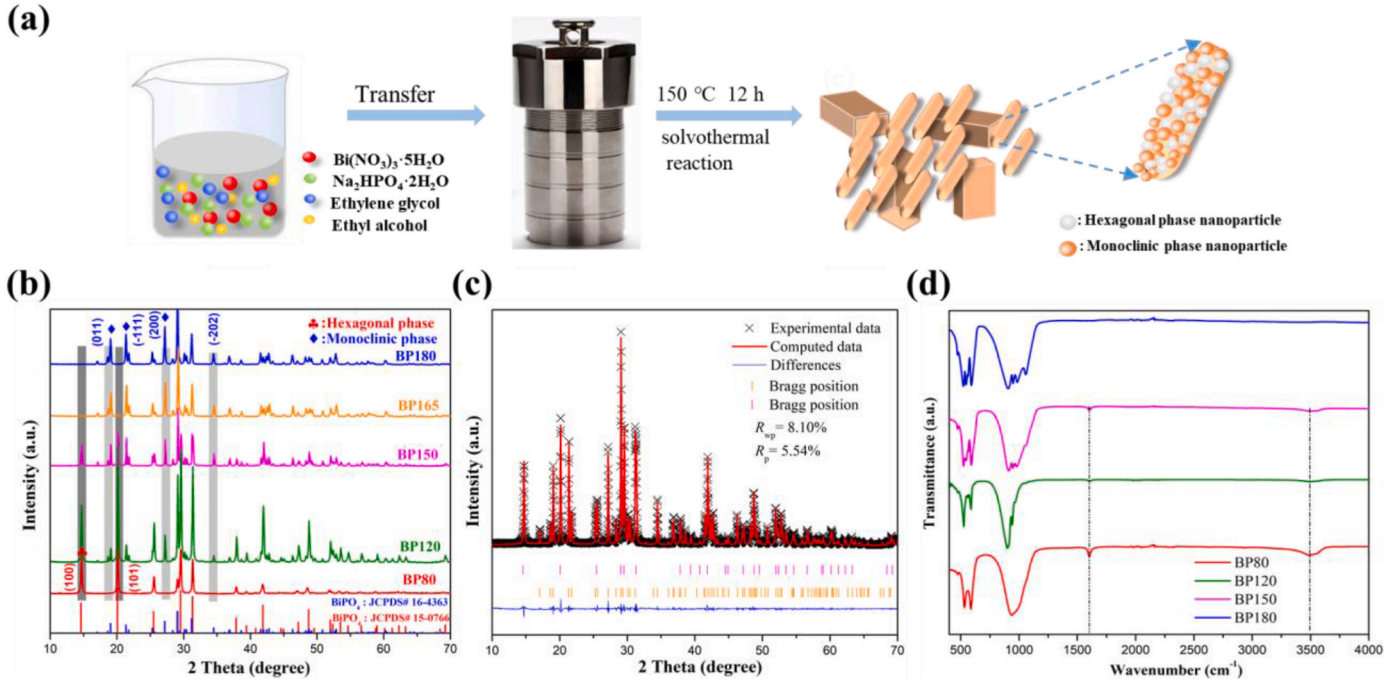

Fig. 1. (a) Schematic diagram for the fabrication of BP150, (b) XRD measurements for five samples, (c) Rietveld refined XRD pattern of BP150 and (d) FTIR spectra of four samples.

distorted due to dehydration. The average P–O bonds length is slightly shorter than the value obtained for hexagonal structure, resulting in the formation of monoclinic crystal phase. Thus, the XRD peaks of BP180 synthesized under the higher reaction temperature match perfectly with the standard pattern of low-temperature monoclinic phase (JCPDS Card No. 16–4363): this is due to the complete transformation of the residual hexagonal phase to low-temperature monoclinic phase during a period of increasing reaction temperature. Full profile Rietveld refinement is performed using WinCSD program package, in order to further confirm the crystal structure and crystal phase composition of BP material, as demonstrated in Fig. 1c and Fig. S3. Refined unit cell parameters of bismuth phosphate samples were listed in Table 1. Apparently, the refined data are in good agreement with the experimental data, which confirms the coexistence of hexagonal and monoclinic phases in the crystal structure of BP120, BP150 and BP165. Rietveld refinement results show that the mass ratio of hexagonal/monoclinic phases in the crystal phase of BP120, BP150 and BP165 is 73 %/27%, 30.8 %/69.2 % and 1 %/99 %, respectively. In order to explore the effect of solvent on the formation of the crystal structure during the synthesis process, BP150-ethanol is synthesized using ethanol as solvent without changing other experimental conditions. However, BP150-ethanol reveals a single monoclinic phase in the XRD pattern (Fig. S4), which indicates that the composition of the solvent plays an important role in the formation of heterogeneous structures.

FTIR spectra of four samples were recorded in the wavenumber region of 500–4000 cm^{-1} to confirm the presence of diverse functional groups and bonding vibrations (see Fig. 1d). Obviously, the characteristic peaks in the range of 500–1300 cm^{-1} of BP120 and BP150 with hexagonal/monoclinic phases are similar to BP180 (monoclinic phase) while in the range of 1600–3600 cm^{-1}, typical peaks of hexagonal phase emerge, similar with BP80. The peaks at 522 and 546 cm^{-1} correspond to Bi–O stretching vibration, while the peak at 593 cm^{-1} for BP150 is assigned to asymmetric bending of δ(O–P–O) and ν_4-bending vibrations of PO_4 [30,38,39]. Besides, the symmetric stretching vibration of the P–O bond due to PO_4 deformation is documented by the peaks in regions of 911, 954 and 982 cm^{-1} [40–42]. The peak observed at 1631 cm^{-1} is attributed to bending vibration δ(H–O–H) of water adsorbed on the surface of samples, whereas hydroxyl (O–H) stretching vibration that coordinated with the bismuth atoms in the hexagonal phase is evidenced at 3493 cm^{-1}. FTIR result further confirms the successful synthesis of $BiPO_4$ with monoclinic/hexagonal crystalline phase heterostructure [38,43,44].

SEM imaging helped to observe the microscopic morphology and structure of the different samples (BP80, BP120, BP150 and BP180), as presented in Fig. 2a–d. BP80 and BP120 synthesized at relatively low temperature appear to have a uniform distribution of nanorod shapes with a length ranging from 200 to 400 nm, as depicted in Fig. 2a–b. Different from BP80 and BP120, BP150 was produced at a moderate temperature, giving rise to a combination of two shapes: nanorods and nanocuboids, with lengths ranging approximately from 100 to 700 nm (Fig. 2c). As depicted in Fig. 2d, BP180 acquired at high temperature is composed of nanostrips and irregular nanocube structures with a significantly increased length (450–750 nm). Moreover, the SEM-EDS elemental mappings of Bi, P and O illustrate a homogeneous distribution of the three elements throughout the sample volume as shown in Fig. 2e and Fig. S5.

Table 1
Refined structural parameters of bismuth phosphate samples.

Sample	Cell parameters					
	a (Å)	b (Å)	c (Å)	α (°)	β (°)	γ (°)
BP80	7.158	7.158	6.636	90	90	120
	6.765	6.951	6.489	90	103.7	90
BP120	6.981	6.981	6.473	90	90	120
BP150	6.997	6.997	6.490	90	90	120
	6.775	6.965	6.498	90	103.7	90
BP165	6.736	6.922	6.462	90	103.7	90
	7.002	7.002	6.491	90	90	120
BP180	6.770	6.960	6.493	90	103.7	90

N_2 adsorption−desorption analysis of BP80, BP150 and BP180 is presented in Fig. 3a–c, aiming to determine their specific surface area and pore size distributions. The results show that all three samples possess similar type IV isotherms with an H3 hysteresis loop, demonstrating the presence of mesoporous structures [45]. The BET surface area of BP150 was calculated to be 17.0 $m^2\ g^{-1}$, which is higher in comparison with BP80 (11.12 $m^2\ g^{-1}$) and BP180 (8.72 $m^2\ g^{-1}$). Moreover, as seen from the pore size distribution diagram (Fig. 3d–f), BP150 has the smallest average pore diameter mainly concentrated at 3.65 and 20.6 nm, further verifying its mesoporous structure. Actually, the average pore sizes of BP80 (concentrated at 3.95 and 27.1 nm) and BP180 (5.3 and 27.1 nm) are larger due to their microstructure differences (see also the TEM discussion below). For BP150, its high specific surface area, small pore diameter, and abundant mesopores, can offer more active sites, shorten the ion diffusion path and accelerate reaction rate during the redox reaction process, being beneficial toward the improvement of the electrochemical performance.

TEM images were acquired to evaluate more precisely the microstructure and the morphological characteristics of the different samples. As illustrated in Fig. 4a, TEM image of BP80 demonstrates a nanorod morphology in accordance with SEM results. Remarkably, the nanorod outer layer has an amorphous structure, probably ascribed to the low reaction temperature used for this sample. The HRTEM image in Fig. 4d (inset for corresponding selected area electron diffraction (SAED) pattern) further confirms the presence of a crystalline structure that tends to become amorphous in the outer layers of the particle. As seen in Fig. 4d, the apparent lattice fringes with an interplanar distance of 0.44 nm correspond well to (101) crystal planes of the $BiPO_4$ hexagonal phase, while the yellow dashed region exhibits a distinct amorphous structure: this is consistent with SAED result showing a combination of broad and diffused halo rings and partially bright diffraction spots. Being somewhat different from the microstructure of BP80, the nanorod morphology of BP150 consists of a bunch of nanoparticles (see Fig. 4b). The causes of the difference in microstructure between BP80 and BP150 may be related to the distinct reaction temperatures used: by applying a gradually increased reaction temperature, the amorphous structure can be fully transformed into monoclinic crystal phase, which is not the same with the hexagonal phase of the host. This conjecture is corroborated by the HRTEM imaging of BP150 (Fig. 4e), where there are several evident lattice fringes in various directions. In that image, the crystal plane spacings of 0.60 and 0.51 nm are assigned to the (100) planes of the hexagonal and (−101) planes of the monoclinic phase, respectively.

This unique heterostructure made up of distinct crystalline phase nanoparticles contributes to the penetration and diffusion of electrolyte ions, generating more active sites as well as rich pores, which greatly promote the electrochemical activity of the BP150 electrode [46]. Given that the reaction temperature gradually increased to 180 °C, the hexagonal phase of BP150 is dehydrated and completely transformed into a monoclinic phase, which can integrate into the original monoclinic phase nanoparticles forming larger structures: this is demonstrated in the TEM image of BP180 in Fig. 4c. The corresponding HRTEM image shows clear lattice fringes with an interplanar distance of 0.41 nm (Fig. 4f), perfectly matching with (−111) planes of the monoclinic phase.

The electrochemical properties of the prepared samples BP80, BP120, BP150, BP165, BP180 and Mixed as anode material for ASCs were investigated in a traditional three-electrode system using 3 M KOH as electrolyte, Pt plate as the counter electrode, and Hg/HgO electrode as the reference electrode. Fig. 5a displays the CV profiles of the BP80, BP120, BP150, BP165, BP180 and Mixed materials at a scan rate of 2 mV s^{-1} in the voltage range of −1∼0 V *vs.* Hg/HgO. Clearly, all six materials have similarly distinct oxidation and reduction peaks, indicating the characteristics of battery-type materials. In addition, the

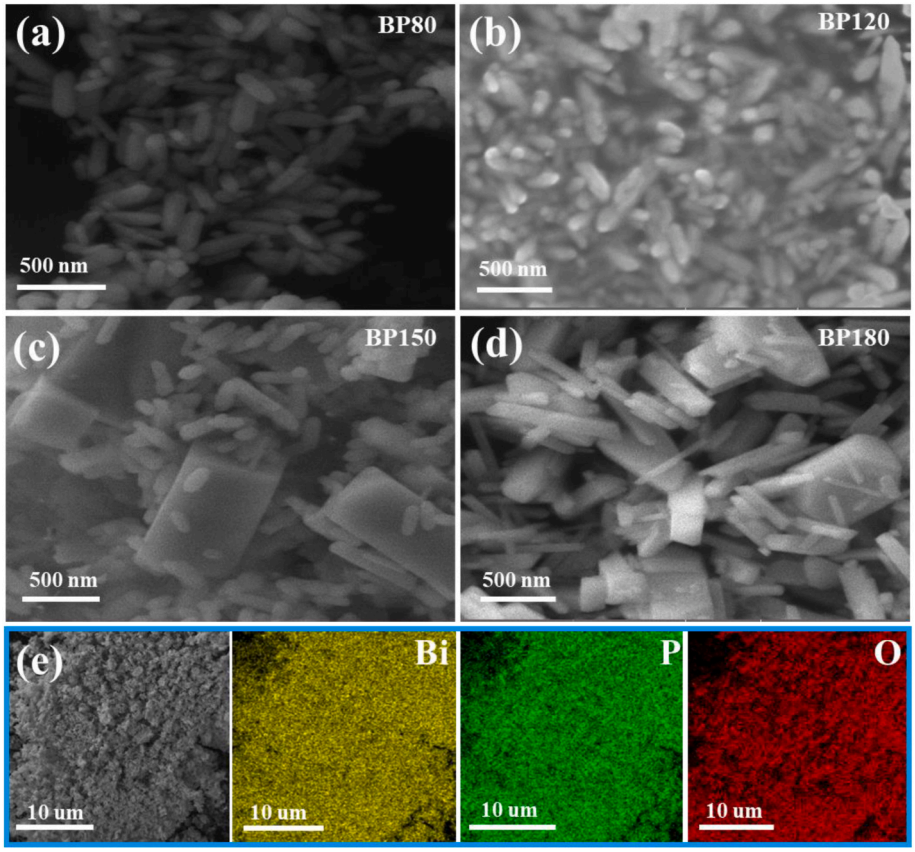

Fig. 2. (a–d) SEM images of BP80, BP120, BP150 and BP180, and (e) elemental mapping of BP150.

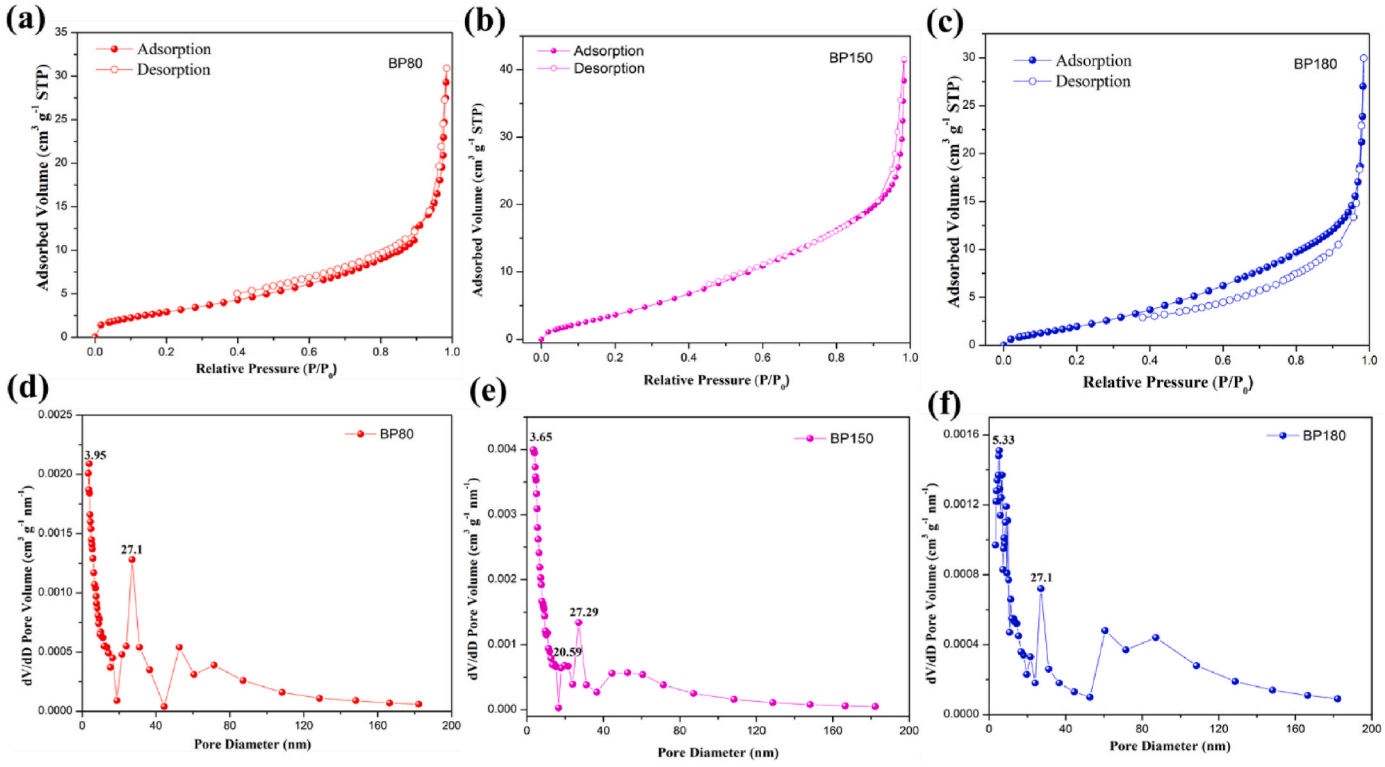

Fig. 3. (a–c) N_2 adsorption-desorption isotherm curves and (d–f) pore size distributions for BP80, BP150 and BP180 materials, respectively.

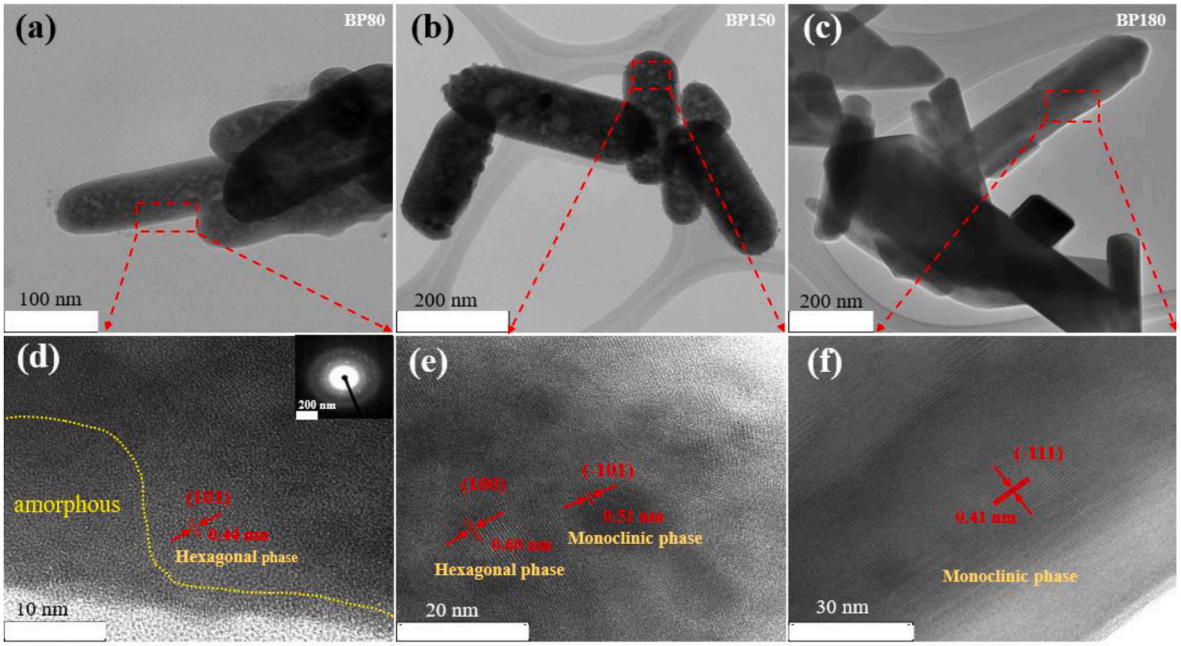

Fig. 4. (a–c) TEM and (d–f) HRTEM images of BP80, BP150 and BP180.

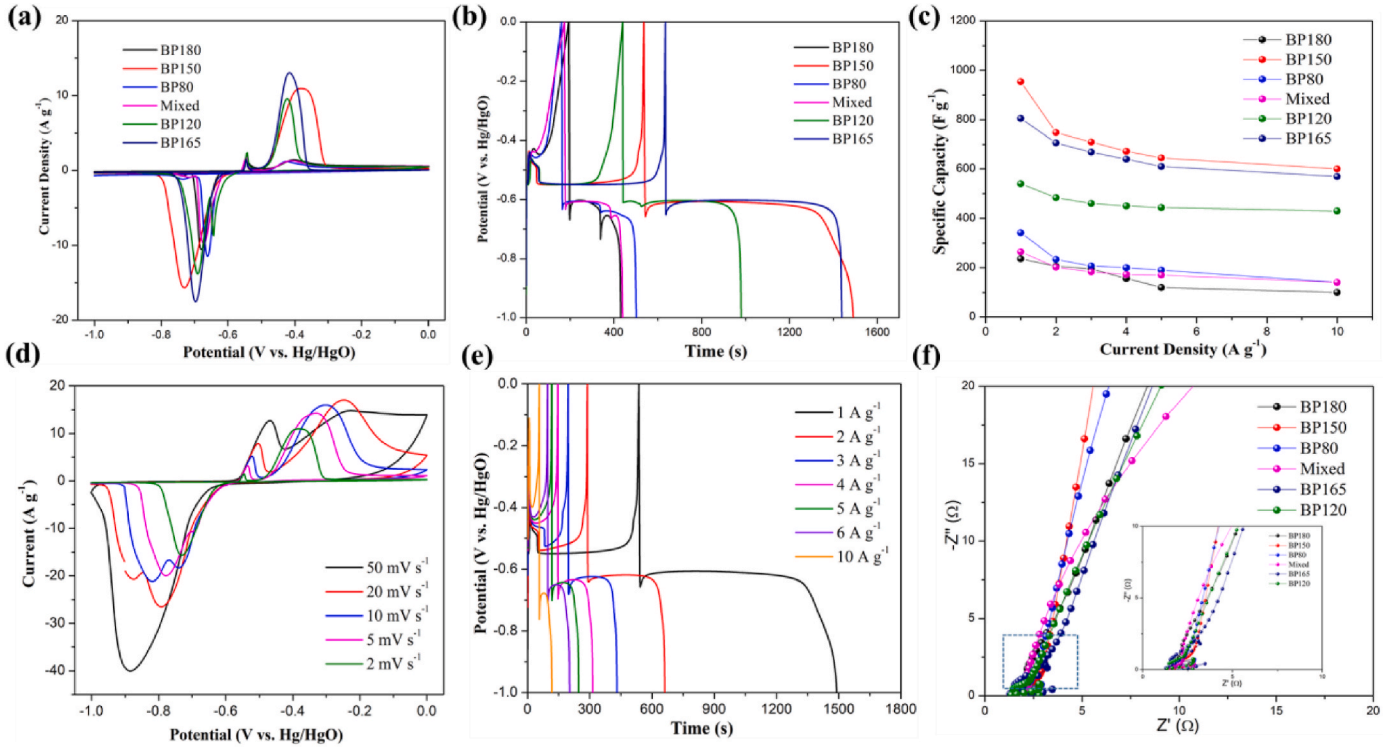

Fig. 5. Electrochemical performance comparison of BP80, BP120, BP150, BP165, BP180 and Mixed, (a) CV curves, (b) GCD curves, (c) the specific capacitance at different current densities, (d–e) CV curves at various scan rates and GCD curves at different current densities of BP150, (f) Nyquist plots of EIS.

integrated area of CV curves can reflect the specific capacitance of the material. Apparently, BP150 has the highest specific capacitance due to its maximum CV integrated area in comparison with the other five materials. The sharp redox peak of BP80, BP120, BP150, BP165, BP180 and Mixed materials in the CV profiles is attributed to the interconversion of Bi^{3+} and active atoms (Bi^0) [38], and the complete reaction mechanism can be analyzed as follows:

Reduction reaction: $BiO_2^- + e^- \rightarrow BiO_2^{2-}$ (ads), $2H_2O + 3BiO_2^{2-} \leftrightarrow 2BiO_2^- + 4OH^- + Bi^0$, $Bi^0 \rightarrow Bi_{metal}$

Oxidation reaction: $Bi_{metal} \rightarrow Bi^+ + e^-$, $3Bi^+ \leftrightarrow Bi^{3+} + 2Bi_{metal}$, $Bi^{3+} + 3OH^- \leftrightarrow Bi(OH)_3$, $Bi(OH)_3 \rightarrow BiOOH + H_2O$ [30,47]

Fig. 5b illustrates the galvanostatic charge-discharge (GCD) curves of all samples at a current density of 1 A g^{-1}, once again verifying the characteristics of battery-type materials, as seen in the voltage drop and charge-discharge platform of GCD curves. Furthermore, the discharge

time can be used to predict the specific capacitance of materials based on Equation (1) (see Experimental section for details), wherein BP150 delivers the highest specific capacitance among all samples. The comparison of CV and GCD curves for all samples manifests the better electrochemical performance of BP150. Furthermore, the discharge-specific capacitance of six samples at different current densities is displayed in Fig. 5c. Apparently, the electrochemical performance of BP150 is much better than that of the other five materials; it displays a superior specific capacitance of 954 (265), 748 (207.8), 709.5 (197.1), 672 (186.7), 645 (179.2) and 600 F g^{-1} (166.7 mAh g^{-1}) at current densities of 1, 2, 3, 4, 5 and 10 A g^{-1}, correspondingly. It can also be observed that there are obvious oxidation peaks and reduction peaks in BP150 CV curves (Fig. 5d), which are similar to the CV curves of BP80, BP120, BP165, BP180 and Mixed (see Figs. S6a–e). As the scan rate is gradually increased, the oxidation peak and the reduction peak shift towards more positive potential and more negative potential, respectively, ascribing to the electrode polarization effects. Even so, the initial CV curve shape is still well-maintained at a large scan rate, indicating good rate performance of BP150, which is in agreement with its following GCD result. As described below (see Fig. 5e), the specific capacitance calculated by GCD curves for BP150 is 954 F g^{-1} at 1 A g^{-1} and the capacitance retention rate is 62.9 % even at the high current density of 10 A g^{-1}. However, the GCD curves of BP80, BP180, BP120, BP165 and Mixed exhibit a relatively short discharge time (see Figs. S7a–e), which corresponds to the specific capacitance of 341.5/236.5/540.4/805.3/265 F g^{-1} (94.9/65.7/150.1/223.7/73.6 mAh g^{-1}), 234/206/483.6/706/202 F g^{-1} (65/57.2/134.3/196.1/56.1 mAh g^{-1}), 207/195/460.2/668.4/183 F g^{-1} (57.5/54.2/127.8/185.7/50.8 mAh g^{-1}), 190/120/444/610/170 F g^{-1} (52.8/33.3/123.3/169.4/47.2 mAh g^{-1}) and 140/100/430/570/140 F g^{-1} (38.9/27.8/119.4/158.3/38.9 mAh g^{-1}) at current densities of 1, 2, 3, 5 and 10 A g^{-1}, respectively. Obviously, the specific capacitances of BP120, BP165 and BP150 materials with heterogeneous structures are significantly higher than those of other single crystalline phase materials. Therefore, it can be inferred that the hexagonal/monoclinic phase heterostructure favors the improvement of the electrochemical activity. As seen from the above results, the electrochemical properties of Mixed sample with a mixed crystal structure are far from remarkable, being rather ordinary.

Compared with the reported literatures in Table 2, the capacitance of BP150 with hexagonal/monoclinic phase heterostructure is quite high and it can be deemed as particularly competitive; this can be attributed to the nanostructure composed of different crystalline phase nanoparticles, which is conducive to promoting the diffusion and reaction of electrolyte ions as well as effectively improve the reaction kinetics.

Electrochemical impedance spectroscopy (EIS) measurements were carried out at a frequency ranging from 0.01 Hz–100 kHz with an amplitude of 10 mV, to assess the ion diffusion kinetics inside the material. As presented in Fig. 5f, the Nyquist plots of all samples are similar in shape, consisting of semi-circles in the high-frequency region and straight oblique lines in the low-frequency region. In general, the internal resistance (R_s) is determined by the intercept between the X-axis and the semicircle of the high-frequency region. The diameter of the semicircle represents the charge transfer impedance (R_{ct}), which is an important parameter used to describe the faradaic charge transfer kinetics occurring at the electrode-electrolyte interface. Moreover, the slope of the line in the low-frequency region can reflect the Warburg impedance that is closely related to the diffusion rate of electrolyte ions within the electrode material. BP150 with hexagonal/monoclinic phase heterostructure has low R_s and a large positive slope (see enlarged image), further indicating its fast faradaic charge-transfer process and good reaction kinetics.

The CV curves of BP150 at small sweep rates of 0.2–1 mV s^{-1} are shown in Fig. 6a, aiming to study more accurately the relationship between peak current (i_p) and sweep rate (v). The fitting results between the peak current and the sweep rate indicate a linear relationship (Fig. 6b), which implies the battery-type material characteristics of BP150. According to their linear relationship, the diffusion coefficient of OH^- (D_{OH-}) within bismuth phosphate electrode can be computed using the following Randles-Sevcik equation (6) [36,37]:

$$i_p = \left(2.69 \times 10^5\right) \times n^{3/2} \times A \times D^{1/2} \times C \times v^{1/2} \quad (6)$$

in which n, A, D, C and v signify transported electrons, working electrode area (cm^2), the diffusion coefficient of OH^- ($cm^2\ s^{-1}$), the concentration of OH^- (mol cm^{-3}) and the sweep rate (mV s^{-1}), respectively. The calculated D_{OH-} of BP80, BP120, BP150, BP165 and BP180 is 8.97 × 10^{-6}/8.24 × 10^{-5}, 2.45 × 10^{-5}/3.95 × 10^{-4}, 6.61 × 10^{-4}/6.94 × 10^{-4}, 2.84 × 10^{-5}/4.22 × 10^{-4} and 6.64 × 10^{-6}/8.33 × 10^{-5} $cm^2\ s^{-1}$, correspondingly. It is clear that BP120, BP150 and BP165 possess large ion diffusion coefficients, indicating the enhancement of the diffusion rate of electrolyte ions in the electrode material thanks to the presence of heterogeneous crystal structure. Besides, the relationship between peak current and sweep rate can be expressed by the following power law so that the energy storage mechanism of BP150 is investigated in detail.

$$i_p = av^b \quad (7)$$

$$\log(|i_p|) = b\log(v) + \log(a) \quad (8)$$

In the above equations, a is a constant, and i_p is the peak current of anodic and cathodic peaks. The b value is used to estimate the diffusion-controlled and surface-controlled processes in the electrochemical reaction process. If $b = 0.5$, it indicates a diffusion-controlled process, which explains the battery-like feature of the prepared material; if $b = 1$, a surface-controlled process is illustrated; if b is between 0.5 and 1, it

Table 2
Comparison of electrochemical performances of BP150 with reported literature works.

Material	Synthesis method	Crystalline phase	Current density	Capacitance	Electrolyte	Reference
$BiPO_4$	sol-gel method	hexagonal phase	2 A g^{-1}	286.28 F g^{-1}	2 M KOH	[38]
			5 A g^{-1}	261.91 F g^{-1}		
$BiPO_4$	hydrothermal	monoclinic phase	1 A g^{-1}	446 F g^{-1}	4 M KOH	[32]
$BiPO_4$-300	microwave	hexagonal phase	1 A g^{-1}	767.14 F g^{-1}	2 M KOH	[48]
$BiPO_4$-600	technique	monoclinic phase		322.14 F g^{-1}		
$BiPO_4$-15	microwave-assisted	hexagonal phase	2 A g^{-1}	435.71 F g^{-1}	2 M KOH	[31]
			5 A g^{-1}	361.91 F g^{-1}		
$BiPO_4$ (H4)	hydrothermal synthesis	monoclinic phase	1 A g^{-1}	480 F g^{-1}	1 M KOH	[30]
			5 A g^{-1}	202 F g^{-1}		
$BiPO_4$ (BPP)	hydrothermal	monoclinic phase	1 A g^{-1}	764.29 F g^{-1}	2 M KOH	[34]
$BiPO_4$	sonochemical synthesis	monoclinic phase	2 A g^{-1}	302 F g^{-1}	1 M KOH	[33]
$BiPO_4$	microwave method	hexagonal phase	2 A g^{-1}	355 F g^{-1}	1 M KOH	[47]
BP150	**solvothermal**	**hexagonal/monoclinic phase**	**1 A g−1**	**954 F g−1**	**3 M KOH**	**This work**
			2 A g−1	**748 F g−1**		
			5 A g−1	**645 F g−1**		
			10 A g−1	**600 F g−1**		

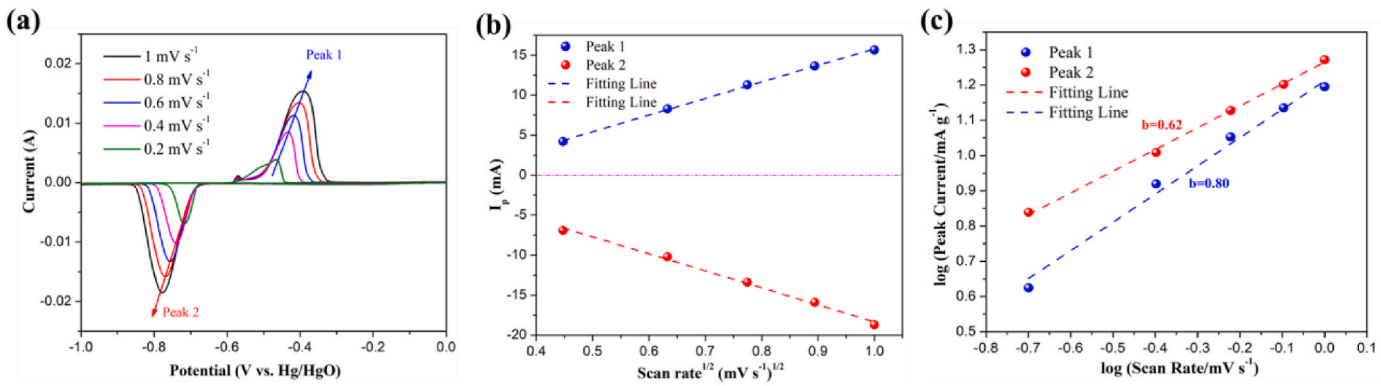

Fig. 6. (a–c) CV curves of BP150 at small scan rates and the relationship between the peak current and scan rate.

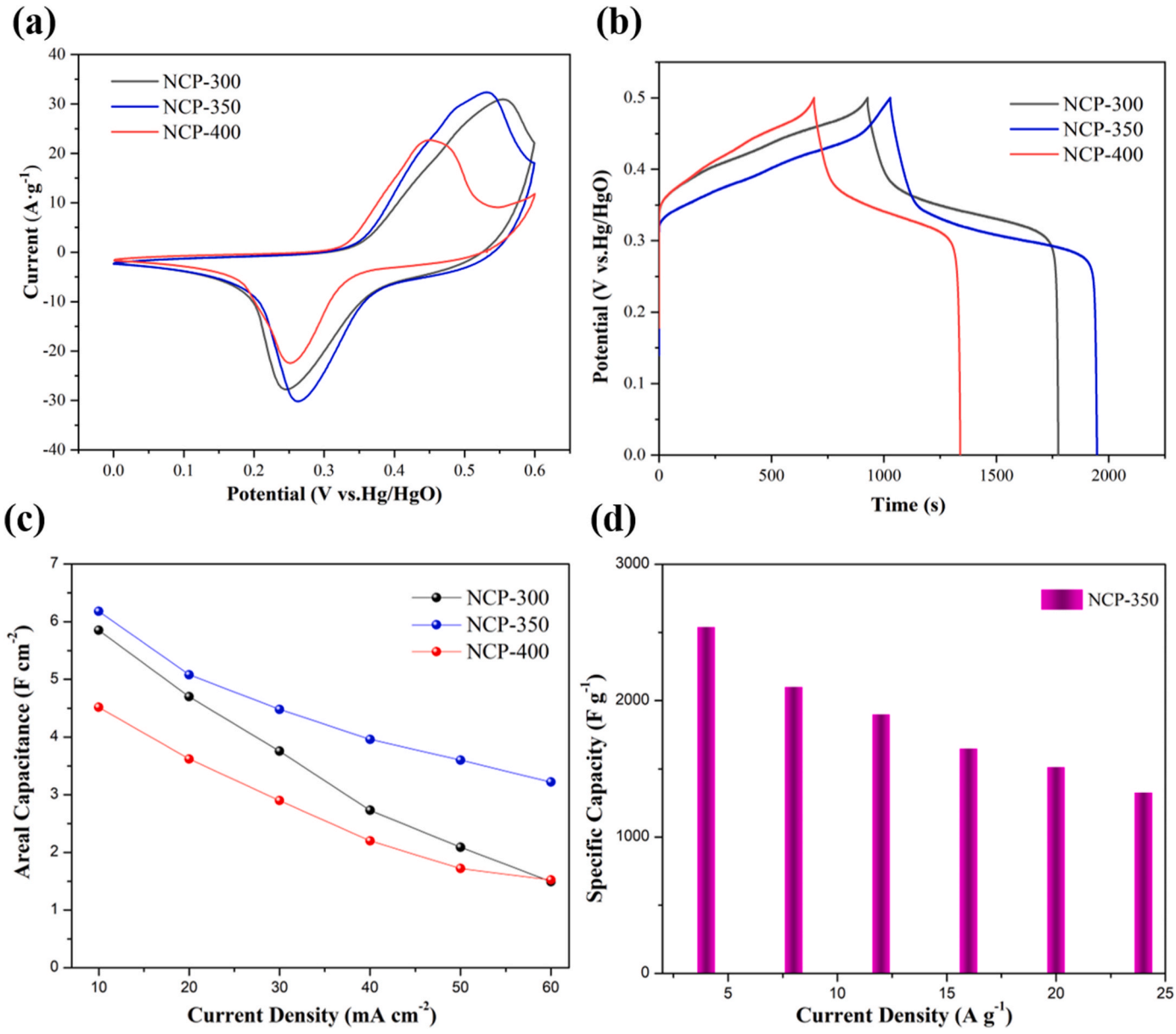

Fig. 7. The comparison of electrochemical performance for NCP-300, NCP-350 and NCP-400 (a) CV curves, (b) GCD curves, (c) The areal-specific capacitances at various current densities, (d) The gravimetric specific capacitance of NCP-350 at different current densities.

shows that both diffusion control and surface control processes take place. The *b* value of BP150 can be derived by the slope of the curve between log($|i_p|$) and log(v) in Fig. 6c. The results show that the *b* value of anodic and cathodic peak for BP150 is 0.8 and 0.62, respectively, which are close to 1, implying that its electrochemical reaction kinetics process is dominated by the surface-controlled process [49].

In order to assemble the aqueous asymmetric supercapacitor equipment which can take into account both high energy density and power density, a high-capacitance cobalt-nickel phosphate material grown directly on NF was synthesized and selected as cathode. The XRD pattern of NCP-350 in Fig. S8 demonstrates the absence of sharp diffraction peaks, which may be due to the formation of small nano-grains from the low calcination temperature. HRTEM imaging for NCP-350 was also performed and the corresponding images are displayed in Figs. S9a–c. It can be observed that numerous small nanocrystals are present in Fig. S9b, where the lattice fringes with an interplanar distance of 0.182 nm and 0.171 nm are in line with the (310) crystal planes of nickel phosphate and (121) crystal planes of cobalt phosphate (Fig. S9b), respectively. The corresponding elemental mapping in Fig. S9c shows that Co, Ni, P and O are evenly dispersed throughout the studied sample. The aforementioned results validate the successful synthesis of cobalt-nickel phosphate micron-sheets. In addition, the N_2 adsorption/desorption isotherm and pore size distribution of NCP-350 are displayed in Figs. S10a–b, in order to study its specific surface area and pore parameters. Clearly, the isothermal curves in the range of 0.45–1.0 p/p_0 reveal a IV-type isotherm with a typical H3 hysteresis loop in Fig. S10a, implying the presence of mesoporous structure of NCP-350 material. The BET surface area of NCP-350 on NF was calculated to be 8.4 $m^2\ g^{-1}$,

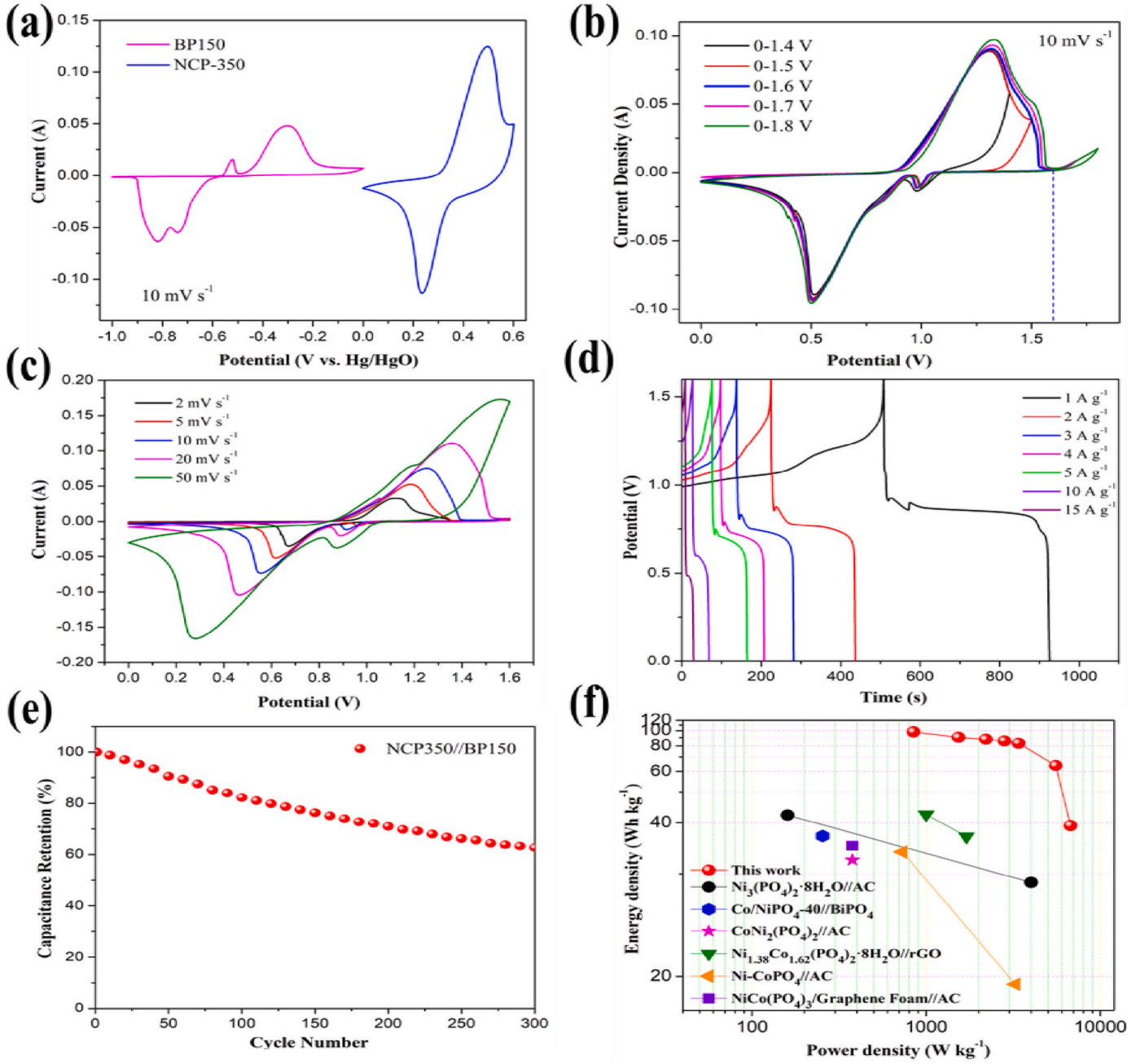

Fig. 8. Electrochemical properties of the assembled aqueous asymmetric supercapacitor of NCP-350//BP150. (a) CV curves of NCP-350 and BP150 in a three-electrode system at 10 mV s^{-1}, (b, c) CV curves at different operation voltage windows and different scan rates, (d) GCD curves, (e) cycling performance and (f) Ragone plot.

and its pore size mainly centered at 3.8 nm, further confirming the mesoporous structure of the obtained material, as shown in the BJH pore size distribution curve (see Fig. S10b). The considerable BET surface area and abundant mesopore structures of NCP-350 can shorten the ion diffusion distance and offer more active sites for redox reaction, contributing to the improvement of electrochemical performance.

The electrochemical performance of NCP-300, NCP-350 and NCP-400 was evaluated under the same conditions as described above for the bismuth phosphate. As shown in Fig. S11, the CV and GCD curves of the three samples demonstrate similar shapes, in which NCP-350 has maximum CV curve integration area and discharge time (see Fig. 7a–b), exhibiting the best electrochemical activity among the three samples. The gravimetric specific capacitance of NCP-350 is up to 3662 F g^{-1} (508.61 mAh g^{-1}) at a current density of 1 A g^{-1}. In addition, the areal-specific capacitances of NCP-300, NCP-350 and NCP-400 at different current densities are presented in Fig. 7c, where the areal specific capacitance of NCP-350 is significantly higher compared to that of the other two materials. As shown in Fig. 7c–d, for NCP-350, when the current densities are 10 (4 A g^{-1}), 20 (8), 30 (12), 40 (16), 50 (20) and 60 (24) mA cm^{-2}, the corresponding specific capacitances are as high as 6.18 (2539.2 F g^{-1}), 5.08 (2100.8), 4.48 (1898.4), 3.96 (1648), 3.6 (1512) and 3.22 (1324.8) F cm^{-2}, respectively, which is associated to the formation of small nanocrystals; these conditions favor the full penetration, diffusion and reaction of the electrolyte ions, leading to an exceptional improvement of the reaction kinetics.

To evaluate its practical application, the aqueous asymmetric supercapacitor was assembled utilizing NCP-350 as the cathode and BP150 as the anode in a 3 M KOH electrolyte. The mass loading of cathode/anode can be calculated by Equation (3) (see Experimental section for details) to balance the charge stored in the electrode, which is ~2.5 mg for NCP-350 and ~5.3 mg for BP150 (7.8 mg for actual total loading). The CV curves involving NCP-350 and BP150 both show sharp redox peaks, as depicted in Fig. 8a, which indicates the battery-type material characteristics. It is crucial to possess a suitable voltage window for an aqueous asymmetric supercapacitor, considering its close relation to practicality and safety issues; therefore its CV curve was recorded in different working voltage windows (see Fig. 8b). Taking into account the appearance of a suddenly increased potential caused by the oxygen evolution reaction in an enlarged voltage window (0~1.7 V and 1.8 V) [47], the appropriate working voltage range for the aqueous asymmetric supercapacitor device is identified in a voltage window from 0 V to 1.6 V. As observed in Fig. 8c, the CV curves of the aqueous asymmetric supercapacitor at different sweep rates express clear, almost symmetrical oxidation and reduction peaks as well as a retained good shape even at a larger sweep rate; this indicates its good reversibility and rate performance during charging and discharge process. The corresponding GCD curves are shown in Fig. 8d, in which the specific capacitance can be calculated at different current densities based on the total loading of the cathode and anode. It delivers a specific capacitance of 260.95 F g^{-1} (115.98 mAh g^{-1}) at a current density of 1 A g^{-1} and even 196.88 F g^{-1} (87.5 mAh g^{-1}) at 15 A g^{-1}. Notably, a good capacity retention rate of 75.45 % relative to the initial capacity at a high current density of 15 A g^{-1} confirms its excellent rate performance, which is in line with CV results. The electrochemical activity of NCP-350//BP150 device is superior or comparable to the performance of asymmetric supercapacitor devices already published in literature reports, as demonstrated in Table S1. The cyclic performance of the aqueous asymmetric supercapacitor with a capacity retention rate of 62.7 % for 300 cycles at a current density of 2 A g^{-1} is shown in Fig. 8e.

The Ragone plot of the NCP-350//BP150 ASC device exhibits a fairly high energy density of 98.17 Wh kg^{-1} at a power density of 846.49 W kg^{-1} when the current density is 1 A g^{-1} (see Fig. 8f). Even at the maximum power density of 6735.43 W kg^{-1}, the ASC device still maintains a high energy density of 39.29 Wh kg^{-1} at 20 A g^{-1}, which is comparable or even far superior to those of most recently reported devices in the literature such as $Ni_3(PO_4)_2{\cdot}8H_2O$//AC (42.1 Wh kg^{-1} at 160 W kg^{-1} and 28.81 Wh kg^{-1} at 4000 W kg^{-1}) [24], Co/N-iPO_4-40//$BiPO_4$ (36.84 Wh kg^{-1} at 254.52 W kg^{-1}) [50], CoN-$i_2(PO_4)_2$//AC (32.2 Wh kg^{-1} at 377.6 W kg^{-1}) [51], $Ni_{1.38}Co_{1.62}(PO_4)_2{\cdot}8H_2O$//rGO (42.3 Wh kg^{-1} at 1000 W kg^{-1} and 36.7 Wh kg^{-1} at 1700 W kg^{-1}) [52], Ni–$CoPO_4$//AC (33.6 Wh kg^{-1} at 730 W kg^{-1} and 19.5 Wh kg^{-1} at 3250 W kg^{-1}) [53], $NiCo(PO_4)_3$/Graphene Foam//AC (34.8 Wh kg^{-1} at 377 W kg^{-1}) [54].

4. Conclusion

In summary, BP150 material with hexagonal/monoclinic crystalline phase heterostructure as anode for ASCs has been synthesized by a feasible, straightforward, eco-friendly solvothermal method. We conducted a comprehensive characterization and analysis to investigate the correlation among temperature, solvent variations and the crystal phase transition of bismuth phosphate material during its synthesis. Additionally, the impact of these factors on the electrochemical performance for BP150 is explored. It can be found that a unique heterogeneous interface consists of two different crystalline phase nanoparticles; this gives rise to more active sites for electrochemical energy storage but also promotes the penetration of electrolyte and shortens the diffusion path of electrolyte ions accompanied by the effective enhancement of reaction kinetics for the BP150 electrode. As a result, the BP150 electrode displays a high specific capacitance of 954 F g^{-1} (265 mAh g^{-1}) at 1 A g^{-1} and the specific capacitance retention is 62.9 % at 10 A g^{-1} compared with the initial capacitance. Furthermore, the aqueous asymmetric supercapacitor assembled with BP150 as anode and NCP-350 as cathode demonstrates a predominant energy density of 98.17 Wh kg^{-1} at 846.49 W kg^{-1} and even at the maximum power density of 6735.43 W kg^{-1}, it maintains a high energy density of 39.29 Wh kg^{-1}. These results indicate that BP150 is a promising anode material for high-performance aqueous energy storage equipment.

CRediT authorship contribution statement

Min Li: Writing – original draft, Investigation, Data curation, Conceptualization. **Mingshu Zhao:** Writing – review & editing, Investigation, Conceptualization. **Bing Wu:** Writing – review & editing, Investigation. **Shuangying Wei:** Writing – review & editing, Investigation. **Stefanos Mourdikoudis:** Writing – review & editing, Investigation. **Vlastimil Mazánek:** Writing – review & editing, Investigation. **Lukas Dekanovsky:** Writing – review & editing, Investigation. **Filipa M. Oliveira:** Writing – review & editing, Investigation. **Jalal Azadmanjiri:** Writing – review & editing, Investigation. **Zdeněk Sofer:** Writing – review & editing, Supervision, Resources, Investigation, Data curation, Conceptualization.

Data availability

The datasets generated during and/or analyzed during the study are accessible via the Zenodo repository: https://zenodo.org/records/12699332.

Declaration of competing interest

The authors declare that they have no known competing financial interests or personal relationships that could have appeared to influence the work reported in this paper.

Data availability

Data will be made available on request.

Acknowledgments

M. L. acknowledge China Scholarship Council (CSC). This work was

supported by ERC-CZ program (project LL2101) from Ministry of Education Youth and Sports (MEYS). The authors acknowledge the assistance provided by the Advanced Multiscale Materials for Key Enabling Technologies project, supported by the Ministry of Education, Youth, and Sports of the Czech Republic. Project No. CZ.02.01.01/00/22_008/0004558, Co-funded by the European Union.

Appendix A. Supplementary data

Supplementary data to this article can be found online at https://doi.org/10.1016/j.mtchem.2024.102194.

References

[1] H. Pang, Y. Ma, G. Li, J. Chen, J. Zhang, H. Zheng, W. Du, Facile synthesis of porous ZnO–NiO composite micro polyhedrons and their application for high power supercapacitor electrode materials, Dalton Trans. 41 (2012) 13284–13291.
[2] P. Simon, Y. Gogotsi, Materials for electrochemical capacitors, Nat. Mater. 7 (2008) 845–854.
[3] M. Winter, R.J. Brodd, What are batteries, fuel cells, and supercapacitors? Chem Rev. 104 (10) (2004) 4245–4270.
[4] L. Sheng, L. Jiang, T. Wei, Q. Zhou, Y. Jiang, Z. Jiang, Z. Liu, Z. Fan, $Fe(CN)_6^{3-}$ ion-modified MnO_2/graphene nanoribbons enabling high energy density asymmetric supercapacitors, J. Mater. Chem. A 6 (2018) 7649–7658.
[5] Z. Wang, Y. Han, Y. Zeng, Y. Qie, Y. Wang, D. Zheng, X. Lu, Y. Tong, Activated carbon fiber paper with exceptional capacitive performance as a robust electrode for supercapacitors, J. Mater. Chem. A 4 (2016) 5828–5833.
[6] M. Yu, X. Cheng, Y. Zeng, Z. Wang, Y. Tong, X. Lu, S. Yang, Dual-doped molybdenum trioxide nanowires: a bifunctional anodefor fiber-shaped asymmetric supercapacitors and microbial fuel cells, Angew. Chem. 55 (2016) 6762–6766.
[7] X. Hu, Z. Deng, J. Suo, Z. Pan, A high rate, high capacity and long life ($LiMn_2O_4$+AC)/$Li_4Ti_5O_{12}$ hybrid battery-supercapacitor, J. Power Sources 187 (2009) 635–639.
[8] H. Lee, H. Lee, Applications of novel carbon/$AlPO_4$ hybrid-coated $H_2Ti_{12}O_{25}$ as a high-performance anode for cylindrical hybrid supercapacitors, ACS Appl. Mater. Interfaces 8 (2016) 28974–28981.
[9] S. Vijayakumar, S. Nagamuthu, G. Muralidharan, Supercapacitor studies on NiO nanoflakes synthesized through a microwave route, ACS Appl. Mater. Interfaces 5 (6) (2013) 2188–2196.
[10] Z. Yu, B. Duong, D. Abbitt, J. Thomas, Highly ordered MnO_2 nanopillars for enhanced supercapacitor performance, Adv. Mater. 25 (24) (2013) 3302–3306.
[11] H. Quan, B. Cheng, Y. Xiao, S.J. Lei, One-pot synthesis of α-Fe_2O_3 nanoplates-reduced graphene oxide composites for supercapacitor application, Chem. Eng. J. 286 (2016) 165–173.
[12] C. Guan, X. Liu, W. Ren, X. Li, C.W. Cheng, J. Wang, Rational design of metal-organic framework derived hollow $NiCo_2O_4$ arrays for flexible supercapacitor and electrocatalysis, Adv. Energy Mater. 7 (12) (2017) 1602391.
[13] C. Zhao, F. Ren, X. Xue, W.T. Zheng, X. Wang, M.L. Chang, A high-performance asymmetric supercapacitor based on $Co(OH)_2$/graphene and activated carbon electrodes, J. Electroanal. Chem. 782 (2016) 98–102.
[14] X. Xiong, D. Ding, D. Chen, G. Waller, Y.F. Bu, Z.X. Wang, M.L. Liu, Three-dimensional ultrathin $Ni(OH)_2$ nanosheets grown on nickel foam for high-performance supercapacitors, Nano Energy 11 (2015) 154–161.
[15] Z. Dai, X. Zang, J. Yang, C.C. Sun, W.L. Si, W. Huang, X.C. Dong, Template synthesis of shape-tailorable NiS_2 hollow prisms as high-performance supercapacitor materials, ACS Appl. Mater. Interfaces 7 (45) (2015) 25396–25401.
[16] K. Krishnamoorthy, G.K. Veerasubramani, S. Radhakrishnan, S.J. Kim, One pot hydrothermal growth of hierarchical nanostructured Ni_3S_2 on Ni foam for supercapacitor application, Chem. Eng. J. 251 (2014) 116–122.
[17] W. Xiong, K. Hu, Z. Li, Y.X. Jiang, Z.G. Li, Z. Li, X.W. Wang, A wearable system based on core-shell structured peptide-Co_9S_8 supercapacitor and triboelectric nanogenerator, Nano Energy 66 (2019) 104149.
[18] D. Sarkar, D. Das, S. Das, A. Kumar, S. Patil, K.K. Nanda, D.D. Sarma, A. Shukla, Expanding interlayer spacing in MoS_2 for realizing an advanced supercapacitor, ACS Energy Lett. 4 (7) (2019) 1602–1609.
[19] X. Zhang, S. Hou, Z. Ding, G. Zhu, H.R. Tang, Y.C. Hou, T. Lu, L.K. Pan, Carbon wrapped CoP hollow spheres for high performance hybrid supercapacitor, J. Alloys Compd. 822 (2020) 153578.
[20] C. An, Y. Wang, Y. Wang, G. Liu, L. Li, F.Y. Qiu, Y.N. Xu, L.F. Jiao, H.T. Yuan, Facile synthesis and superior supercapacitor performances of Ni_2P/rGO nanoparticles, RSC Adv. 3 (14) (2013) 4628–4633.
[21] B. Liang, Z. Zheng, M. Retana, K. Lu, T. Wood, Y.L. Ai, X.T. Zu, W.L. Zhou, Synthesis of FeP nanotube arrays as negative electrode for solid-state asymmetric supercapacitor, Nanotechnology 30 (29) (2019) 295401.
[22] C. Yang, L. Dong, Z. Chen, H.B. Lu, High-performance all-solid-state supercapacitor based on the assembly of graphene and manganese (II) phosphate nanosheets, J. Phys. Chem. C 118 (33) (2014) 18884–18891.
[23] H. Shao, N. Padmanathan, D. McNulty, C. O'Dwyer, K.M. Razeeb, Supercapattery based on binder-free $Co_3(PO_4)_2{\cdot}8H_2O$ multilayer nano/microflakes on nickel foam, ACS Appl. Mater. Interfaces 8 (42) (2016) 28592–28598.
[24] G.C. Zhang, M. Feng, Q. Li, Z. Wang, Z.X. Fang, Z.M. Niu, N.R. Qu, X.Y. Fan, S. H. Li, J.M. Gu, J.D. Wang, D.S. Wang, High energy density in combination with high cycling stability in hybrid supercapacitors, ACS Appl. Mater. Interfaces 14 (2) (2022) 2674–2682.
[25] L.Q. Fan, G.J. Liu, J.H. Wu, L. Liu, J.M. Lin, Y.L. Wei, Asymmetric supercapacitor based on graphene oxide/polypyrrole composite and activated carbon electrodes, Electrochim. Acta 137 (2014) 26–33.
[26] S. Khan, A. Majid, R. Raza, Synthesis of PEDOT: PPy/AC composite as an electrode for supercapacitor, J. Mater. Sci. Mater. Electron. 31 (16) (2020) 13597–13609.
[27] S. Vadivel, D. Maruthamani, M. Kumaravel, B. Saravanakumar, B. Paul, S.S. Dhar, K. Saravanakumar, V. Muthuraj, Supercapacitors studies on $BiPO_4$ nanoparticles synthesized *via* a simple microwave approach, J. Taibah Univ. Medical Sci. 11 (4) (2017) 661–666.
[28] D. Wang, Z. Fu, Y. Xu, X.L. Guo, F. Wang, W.J. Sun, P. Yin, Z.L. Yang, L.X. Yang, Uniform $BiPO_4$ nanosheets as an excellent electrode material for supercapacitors, Mater. Lett. 281 (2020) 128610.
[29] S. Vadivel, A.N. Naveen, J. Theerthagiri, et al., Solvothermal synthesis of $BiPO_4$ nanorods/MWCNT (1D-1D) composite for photocatalyst and supercapacitor applications, Ceram. Int. 42 (12) (2016) 14196–14205.
[30] V.D. Nithya, R.K. Selvan, L. Vasylechko, Hexamethylenetetramine assisted hydrothermal synthesis of $BiPO_4$ and its electrochemical properties for supercapacitors, J Phys Chem Solids 86 (2015) 11–18.
[31] P. Chand, A. Joshi, V. Singh, High performance of facile microwave-assisted $BiPO_4$ nanostructures as electrode material for energy storage applications, Mater. Sci. Semicond. Process. 122 (2021) 105472.
[32] A. Joshi, P. Chand, V. Singh, Optical and electrochemical performance of hydrothermal synthesis of $BiPO_4$ nanostructures for supercapacitor applications, Mater. Today: Proc. 32 (2020) 498–503.
[33] V.D. Nithya, B. Hanitha, S. Surendran, D. Kalpana, R.K. Selvan, Effect of pH on the sonochemical synthesis of $BiPO_4$ nanostructures and its electrochemical properties for pseudocapacitors, Ultrason. Sonochem. 22 (2015) 300–310.
[34] A. Joshi, P. Chand, Electrochemical performance of surfactant based $BiPO_4$ nanostructures for energy storage applications, Mater. Today: Proc. 43 (2021) 3225–3230.
[35] J. Zhang, H. Sade, Y. Zhao, A.T. Murdock, A. Bendavid, J.-P. Lellouche, G. Wang, Z. Han, Conformal carbon coating on WS_2 nanotubes for excellent electrochemical performance of lithium-ion batteries, Nanotechnology 30 (2019) 035401.
[36] C.C. Lee, F.S. Omar, A. Numan, N. Duraisamy, K. Ramesh, S. Ramesh, An enhanced performance of hybrid supercapacitor based on polyaniline-manganese phosphate binary composite, J. Solid State Electrochem. 21 (2017) 3205–3213.
[37] J. Theerthagiri, K. Thiagarajan, B. Senthilkumar, Z. Khan, R.A. Senthil, P. Arunachalam, J. Madhavan, M. Ashokkumar, Synthesis of hierarchical cobalt phosphate nanoflakes and their enhanced electrochemical performances for supercapacitor applications, ChemistrySelect 2 (1) (2017) 201–210.
[38] P. Chand, A. Joshi, S. Saini, S. Lal, Sol-gel assisted morphology and phase dependent electrochemical performance of $BiPO_4$ nanostructures for energy storage applications, J. Alloys Compd. 899 (2022) 163315.
[39] M.H. Fulekar, A. Singh, D.P. Dutta, M. Royc, A. Ballald, A.K. Tyagi, Ag incorporated nano $BiPO_4$: sonochemical synthesis, characterization and improved visible light photocatalytic properties, RSC Adv. 4 (20) (2014) 10097–10107.
[40] J. Di, J. Xia, S. Yin, H. Xu, L. Xu, Y.G. Xu, M.Q. He, H.M. Li, Preparation of sphere-like gC_3N_4/BiOI photocatalysts *via* a reactable ionic liquid for visible-light-driven photocatalytic degradation of pollutants, J. Mater. Chem. A 2 (15) (2014) 5340–5351.
[41] H. Assaaoudi, A. Ennaciri, A. Rulmont, Vibrational spectra of hydrated rare earth orthophosphates, Vib. Spectrosc. 25 (1) (2001) 81–90.
[42] Y. Liu, M. Sun, Y. Liu, G.Q. Chen, X. Zhang, Effects of aging time on phase, morphology, and luminescence by two-photon processes of $BiPO_4$: Er^{3+}, Yb^{3+} in the solvothermal synthesis, Opt, Mater. 45 (2015) 32–36.
[43] V.D. Nithya, Phase and shape dependent electrochemical properties of $BiPO_4$ by PVP assisted hydrothermal method for pseudocapacitors, RSC Adv. 4 (2014) 65184–65194.
[44] Y. Li, Y. Wang, Y. Huang, J. Cao, W. Ho, S. Lee, C. Fan, Controllable synthesis of phosphate-modified $BiPO_4$ nanorods with high photocatalytic activity: surface hydroxyl groups concentrations effects, RSC Adv. 5 (2015) 99712–99721.
[45] H. Wu, J. Guo, D. Yang, Facile autoreduction synthesis of core-shell Bi-Bi_2O_3/CNT with 3-dimensional neural network structure for high-rate performance supercapacitor, J. Mater. Sci. Technol. 47 (2020) 169–176.
[46] L. Su, L.J. Gao, Q.H. Du, Construction of $NiCo_2O_4$@MnO_2 nanosheet arrays for high-performance supercapacitor: highly cross-linked porous heterostructure and worthy electrochemical double-layer capacitance contribution, J. Alloys Compd. 749 (2018) 900–908.
[47] A. Joshi, S. Saini, P. Chand, Electrochemical behaviour of temperature-based bismuth phosphate nanostructures for energy storage application, Chem. Phys. Lett. 804 (2022) 139898.
[48] P. Chand, A. Joshi, V. Singh, Impact of phase segregation on optical and electrochemical property of $BiPO_4$ nanostructures for energy storage applications, J. Mater. Sci. Mater. Electron. 31 (19) (2020) 16867–16881.
[49] Y. Shao, M.F. El-Kady, J. Sun, Y.G. Li, Q.H. Zhang, M.F. Zhu, H.Z. Wang, B. Dunn, R.B. Kaner, Design and mechanisms of asymmetric supercapacitors, Chem. Rev. 118 (18) (2018) 9233–9280.
[50] D. Wang, Y. Wang, Z. Fu, Y.B. Xu, L.X. Yang, F. Wang, X.L. Guo, W.J. Sun, Z. L. Yang, Cobalt–nickel phosphate composites for the all-phosphate asymmetric supercapacitor and oxygen evolution reaction, ACS Appl. Mater. Interfaces 13 (29) (2021) 34507–34517.
[51] L. Tao, J. Li, Q. Zhou, H.L. Zhu, G. Hu, J.P. Huang, Composition, microstructure and performance of cobalt nickel phosphate as advanced battery-type capacitive material, J. Alloys Compd. 767 (2018) 789–796.

[52] S.J. Marje, V.V. Patil, V.G. Parale, H. Park, P.A. Shinde, J.L. Gunjakar, C. D. Lokhande, U.M. Patil, Microsheets like nickel cobalt phosphate thin films as cathode for hybrid asymmetric solid-state supercapacitor: influence of nickel and cobalt ratio variation, Chem. Eng. J. 429 (2022) 132184.

[53] A. Numan, F. Bibi, F.S. Omar, Sami Ullah, O.A. Al-Hartomy, M. Khalid, Harvesting enhanced electrochemical performance of mixed structured nickel cobalt phosphate for energy storage application, J. Alloys Compd. 927 (2022) 167031.

[54] A.A. Mirghni, K.O. Oyedotun, B.A. Mahmoud, A. Bello, S.C. Ray, N. Manyala, Nickel-cobalt phosphate/graphene foam as enhanced electrode for hybrid supercapacitor, Compos. B Eng. 174 (2019) 106953.